Diverging responses of terrestrial ecosystems to water stress after disturbances

Meng Liu[1,2], Josep Peñuelas[3,4], Anna T. Trugman[5], German Vargas G.[1,2], Linqing Yang[1,2], William R. L. Anderegg[1,2]

[1]School of Biological Sciences, University of Utah, Salt Lake City, UT, USA

[2]Wilkes Center on Climate Science and Policy, University of Utah, Salt Lake City, UT, USA

[3]CREAF, Cerdanyola del Vallès, Barcelona, Catalonia, Spain

[4]CSIC, Global Ecology Unit CREAF-CSIC-UAB, Bellaterra, Barcelona, Catalonia, Spain

[5]Department of Geography, University of California Santa Barbara, Santa Barbara, CA, USA

Abstract

Terrestrial ecosystems are major carbon (C) pools and sequester approximately 20% of anthropogenic C emissions[1]. However, the increasing frequency and intensity of climate-sensitive disturbances[2,3], such as droughts and wildfires, are threatening long-term terrestrial C uptake. Although direct effects of disturbances (e.g. decreasing C uptake during droughts) are well-documented, indirect effects such as long-term changes in the sensitivity of ecosystem productivity to climate variation remain unknown. We quantify the changes in the sensitivity of terrestrial gross primary production (GPP) to water stress before and after severe droughts and fires. We find divergent changes in sensitivity among regions across the globe, where dry regions, such as Australia and western North America, have increased sensitivity, while wet regions like tropical forests have decreased sensitivity. Water availability, solar radiation, nutrient availability, and biodiversity are the main drivers mediating the changes in sensitivity. It takes approximately 4~5 years for the sensitivity to recover after disturbances, but the increasing frequency of disturbances threatens the recovery of the sensitivity. Our results reveal strong cross-system discrepancies in ecosystem responses to disturbances and highlight the increasing sensitivity of ecosystem productivity to water stress in dry regions, indicating more vulnerable ecosystems in drylands in future climates.

Main

Terrestrial vegetation sequesters approximately 1.9 Pg carbon (C) per year (net C sink) and stores 450 Pg C[1] across the globe, counterbalancing ~20% of human C emissions annually. Disturbances exacerbated by climate change, such as droughts and wildfires, decrease ecosystem productivity[4,5], increase tree mortality[6], and compromise the capacity of terrestrial C sinks[7,8]. Climate change is projected to drive more frequent and severe disturbances in the following decades[2], which will cause substantial threats to terrestrial C uptake and dramatically affect the global C cycle. Terrestrial gross primary production (GPP) directly measures photosynthetic productivity and vegetation C uptake and plays a key role in regulating the capacity of terrestrial C sinks, but it is strongly impacted by climate extremes and disturbances[4,9,10]. Hence, monitoring the long-term dynamics of terrestrial GPP and understanding how ecosystem C uptake responds to disturbances may offer critical insights into how climate change will impact terrestrial ecosystems, C uptake, and land C sinks.

Disturbances have both direct and indirect effects on ecosystem productivity. GPP tends to decrease substantially during disturbances[4], which is a direct effect. On the other hand, there are indirect effects, which are defined as the long-term changes in the sensitivity of ecosystem productivity to climate stressors after disturbances. The indirect effects can persist for several years due to potential physiological damage, compositional changes, and legacy effects[11]. The change in the sensitivity of GPP to water stress after disturbances captures the subsequent vulnerability of ecosystems to water deficits. A higher sensitivity of GPP to water stress implies a higher vulnerability to drought and less C uptake under dry conditions. The sensitivity of ecosystem productivity (i.e. GPP) to water stress can be influenced by many factors[12–15], such as climate, soil, community composition and structure, and physiological traits. A previous study has also found that the sensitivity of GPP to water stress is notably impacted by disturbances, where the sensitivity increased significantly after severe droughts and fires across the conterminous United States[16]. However, the patterns of the change in the sensitivity of GPP to water stress at the global scale due to disturbances (i.e. droughts and fires) remain unknown. Whether GPP becomes less or more sensitive to water stress globally after disturbances is still unclear. Quantifying the indirect effects of disturbances on ecosystem GPP at the global scale is

important for illuminating the future of terrestrial ecosystem productivity and C sequestration in a rapidly changing climate.

We investigated the changes in the sensitivity of GPP to water stress after disturbances (severe droughts and fires) and quantified the time needed for the sensitivity to recover. We hypothesized that the sensitivity of GPP to water stress would increase after disturbances, but high ecosystem diversity might decrease the sensitivity due to the buffering effects of trait diversity. This study focused on high severity droughts because low severity droughts generally had limited impacts on ecosystem functioning and C uptake. We used an ensemble of five long-term remote sensing based GPP products (see Methods) and regressed GPP against drought indices, such as the Palmer Drought Severity Index (PDSI)[17] and the Standardized Precipitation–Evapotranspiration Index (SPEI)[18]. We estimated the sensitivity of GPP to water stress (hereafter 'drought sensitivity') and compared the sensitivity before and after disturbances. We also analyzed the patterns of the changes in drought sensitivity at both the global and the regional scales. We leveraged random forest regression[19] to illuminate the contribution of climatic, nutrient, and biological variables (e.g. precipitation, temperature, solar radiation, nutrient availability, and biodiversity) to the change in drought sensitivity. We finally quantified the recovery time for drought sensitivity to revert to the pre-disturbance condition. We asked three questions: 1) How does drought sensitivity change after disturbances at the global scale? 2) What are the dominant drivers of the change in drought sensitivity? 3) How long does drought sensitivity need to revert to the pre-disturbance level and how does this compare to current and future disturbance return intervals?

Change in drought sensitivity globally

The drought sensitivity did not change significantly at the global scale after severe droughts but increased significantly after fires. Across the globe, the changes in drought sensitivity were highly heterogeneous among regions. The global mean change in sensitivity (Δk) after severe droughts was -0.23 ± 0.55 g C m^{-2} (mean ± standard error), which was not significant (Fig. 1a). Western North America was dominated by increased sensitivity ($\Delta k > 0$) after severe droughts, while South America had decreased sensitivity ($\Delta k < 0$), particularly in tropical rainforests. Tropical regions in Africa and southeastern Asia and boreal regions in Europe also had decreased sensitivity. Other

regions, such as southern Africa, central Eurasia, and Australia, had increased sensitivity. The latitudinal variation of the change in drought sensitivity in Fig. 1a also indicated decreased sensitivity in tropical regions and increased sensitivity at mid-latitudes of the Northern and Southern Hemispheres. Sensitivity in Fig. 1b increased significantly after fires by 1.88 ± 0.71 g C m^{-2}, and there were also differences in the changes in sensitivity among regions. We separated the five remote sensing based GPP products used in this study and obtained similar results (Extended Data Fig. 1), where the changes in sensitivity were not significant after severe droughts except the result from the Breathing Earth System Simulator (BESS) GPP[20] data (Δk increased significantly). The sensitivity for fires increased in all GPP products, and the P-model GPP[21] and the BESS GPP had significantly increased sensitivity.

When using remote sensing GPP and SPEI, the results for the change in sensitivity (Extended Data Fig. 2a and b) are comparable to those shown in Fig. 1, where the sensitivity did not change significantly after severe droughts but increased significantly after fires, with changes of 0.18 ± 1.59 and 3.63 ± 1.81 g C m^{-2}, respectively. Australia and southern Africa exhibited increased sensitivity, while tropical forests showed decreased sensitivity after severe droughts. When using GPP data derived from land-surface models in TRENDY[1] and PDSI, the sensitivity decreased significantly at the global scale by −2.60 ± 0.83 g C m^{-2} after severe droughts (Extended Data Fig. 2c), particularly in tropical regions, Africa, and Australia. The change in sensitivity after fires was negative and not significant (Extended Data Fig. 2d), at −0.86 ± 0.98 g C m^{-2}. The decrease in sensitivity in Australia was evident after fires. The decreased sensitivity from model-based GPP data implied that land-surface models underestimated the sensitivity of GPP to water stress after disturbances, perhaps due to the overestimation of water-use efficiency (WUE) in response to rising CO_2 concentrations. Previous research[22] has shown that global WUE has saturated in the past two decades because of increasing vapor pressure deficit. The land-surface models may not adequately capture this change, potentially increasing the uncertainty in the projections of future ecosystem productivity and terrestrial C sinks.

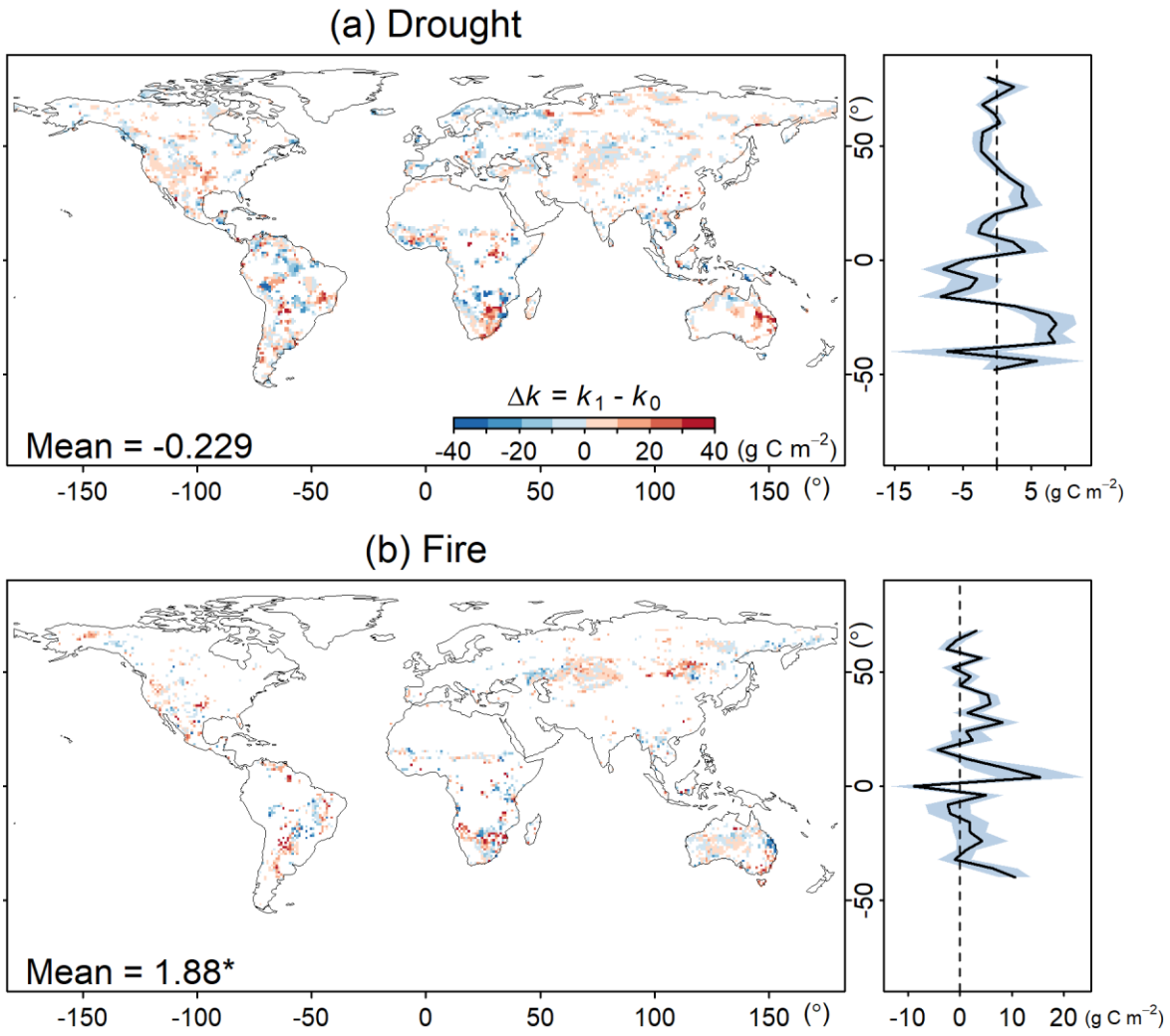

Fig. 1 Large spatial heterogeneities in the change in drought sensitivity after disturbances. (**a**-**b**) Changes in sensitivity (Δk) after (**a**) severe droughts and (**b**) fires using the ensemble mean of remote sensing based GPP data (regressed by PDSI). k_1 and k_0 are the post- and pre- disturbance sensitivity, respectively. There are 23172 and 5358 pixels for drought and fire, respectively. The distributional maps are aggregated to 1° for visual display, and red values indicate increases in sensitivity. The mean changes in sensitivity are derived from a generalized least squares (GLS) model. The shading in the latitudinal plots represents one standard error. *, $p < 0.05$.

Dry and wet regions had divergent changes in drought sensitivity after disturbances. Hyperarid, arid, and semi-arid regions had increased sensitivity after severe droughts, but dry sub-humid and humid regions had decreased sensitivity (Fig. 2a and Extended Data Fig. 3). The increased sensitivity in arid regions was significant, at 2.74 ± 0.86 g C m^{-2} (Fig. 2a and Table S1 in

the Supplement). The contrasting changes in sensitivity accounted for the overall muted signals of the change in sensitivity at the global scale (Fig. 1a). Sensitivity for fires increased significantly in hyperarid, semi-arid, and dry sub-humid regions by 3.49 ± 1.11, 3.49 ± 1.20, and 4.01 ± 1.64 g C m^{-2}, respectively. The results were comparable when separating the five remote sensing based GPP products. Most GPP products indicated significantly increased sensitivity in arid regions after droughts, except the near-infrared reflectance of vegetation (NIRv) based GPP[23] (Fig. 2b and Table S2 in the Supplement). Sensitivity also increased significantly in semi-arid regions when using the BESS GPP. Sensitivity decreased in dry sub-humid and humid regions for most products (except the BESS GPP), and the decrease was significant when using the P-model GPP for humid regions. Sensitivity increased significantly after fires (Fig. 2c) in hyperarid regions except the result from the NIRv GPP. There were also some significant increases in sensitivity in arid, semi-arid, and dry sub-humid regions when using the P-model and the BESS GPP. Sensitivity decreased in humid regions insignificantly when using the Global Land Surface Satellite (GLASS) GPP[24], the revised eddy-covariance model of light-use efficiency (EC-LUE) GPP[25], and the NIRv GPP.

We found similar results when using remote sensing GPP and SPEI (Extended Data Fig. 4a), where drought sensitivity increased significantly by 9.91 ± 2.49 g C m^{-2} in arid regions after severe droughts. For fires, the sensitivity increased significantly in semi-arid and dry sub-humid regions, at 8.43 ± 2.69 and 9.83 ± 4.49 g C m^{-2}, respectively. The changes in sensitivity were negative in humid regions for both droughts and fires. When examining GPP simulated by land-surface models and using PDSI data, the sensitivity decreased in all aridity levels after severe droughts (Extended Data Fig. 4b), and the decrease was significant in humid regions, at −2.58 ± 0.93 g C m^{-2}. For fires, the sensitivity changes were not significant in all aridity levels in Extended Data Fig. 4b. These results were consistent with the changes in sensitivity after severe droughts and fires at the global scale using model-based GPP data (Extended Data Fig. 2c and d).

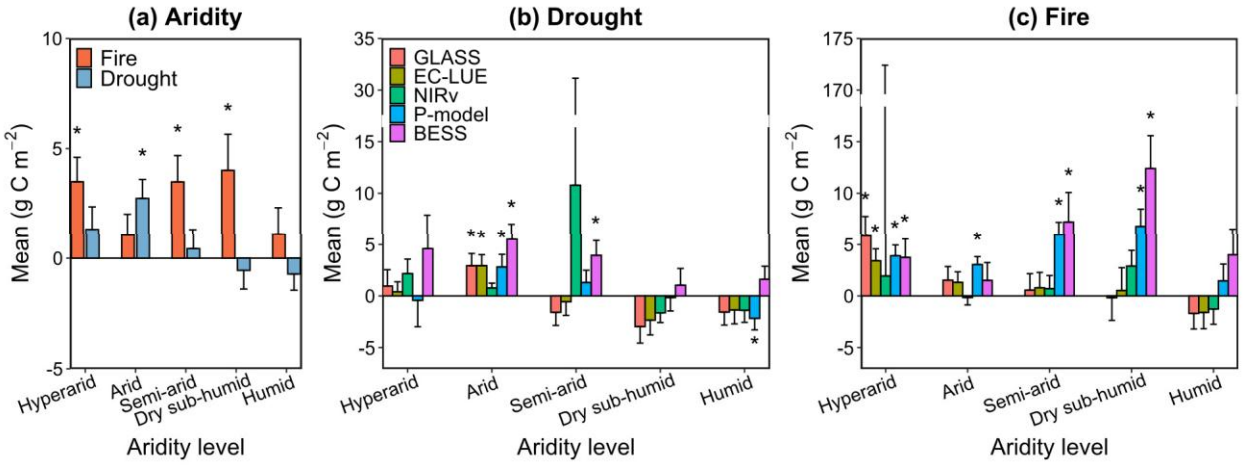

148

149 **Fig. 2 Drought sensitivity in dry regions increased significantly after disturbances.** (**a**) The
150 changes in sensitivity at various aridity levels after severe droughts and fires using the ensemble
151 of remote sensing GPP products (regressed by PDSI). (**b**-**c**) The changes in sensitivity after (**b**)
152 severe droughts and (**c**) fires using a single GPP product (regressed by PDSI). Error bars are one
153 standard error. *, $p < 0.05$ based on the GLS models.

154 **Drivers of changes in drought sensitivity**

155 Climate was the main driver associated with the changes in drought sensitivity after disturbances.
156 We used random forest regression to identify the contributions of different variables and
157 removed highly correlated variables before training the model (see Methods). For severe
158 droughts, the random forest regression model explained 60% of the variation in the change in
159 sensitivity (Fig. 3a). The importance of climatic, nutrient, and biological variables (Fig. 3b) in the
160 random forest model was 65%, 21%, and 14%, respectively. Water availability (Trend.PDSI, AI -
161 aridity index, and Trend.sm), solar radiation (Mean.Srad, and Trend.Srad), and CO_2 concentration
162 (Trend.CO_2) were the main climatic drivers affecting the change in drought sensitivity (Fig. 3b). A
163 high availability of water, i.e. increasing trends of PDSI and soil moisture content and high AI
164 values, was associated with decreased sensitivity (Extended Data Fig. 5a, b, and h), consistent
165 with the results in Fig. 2a (where dry and wet regions had increased and decreased sensitivities,
166 respectively). High downward surface shortwave solar radiation was associated with increased
167 sensitivity (Extended Data Fig. 5c and f), perhaps due to the increased photosynthetic rate (and
168 demand for water) under high levels of solar radiation. A high trend of CO_2 concentration was

initially associated with the decrease in sensitivity as shown in Extended Data Fig. 5e, and then promoted the increase in sensitivity after a rate of ~1.7 ppm y^{-1}. The nutrient and biological variables, such as nitrogen deposition (N.deposition) and biodiversity, also affected the change in sensitivity. Drought sensitivity decreased with the initial increase in N.deposition, but increased after ~300 milligram N m^{-2} (Extended Data Fig. 5d). We hypothesize that the increases in sensitivity at high levels of N.deposition may be due to the constraints of other nutrients, such as phosphorus. High plant biodiversity contributed to the decrease in sensitivity (Extended Data Fig. 5g), implying that high species diversity helped to increase the resistance of ecosystems to disturbances.

The random forest model explained only 37% of the variation in the change in drought sensitivity after fires (Fig. 3c). The importance of the climatic, nutrient, and biological variables (Fig. 3d) was 55%, 24%, and 21%, respectively. N.deposition was the most important driver, followed by the trends of downward surface shortwave solar radiation and PDSI (Fig. 3d). The patterns of the change in sensitivity (Extended Data Fig. 6), along with these predictors, were less clear than after severe droughts. For example, sensitivity first increased with N.deposition, then decreased, and finally increased again (Extended Data Fig. 6a), which reveals the complex and mixed responses to nutrients. Sensitivity increased with the increasing trend of downward surface shortwave solar radiation (Extended Data Fig. 6b), comparable to the results for drought. Less clear driving variables may partly explain why the R^2 of the random forest model in Fig. 3c was low.

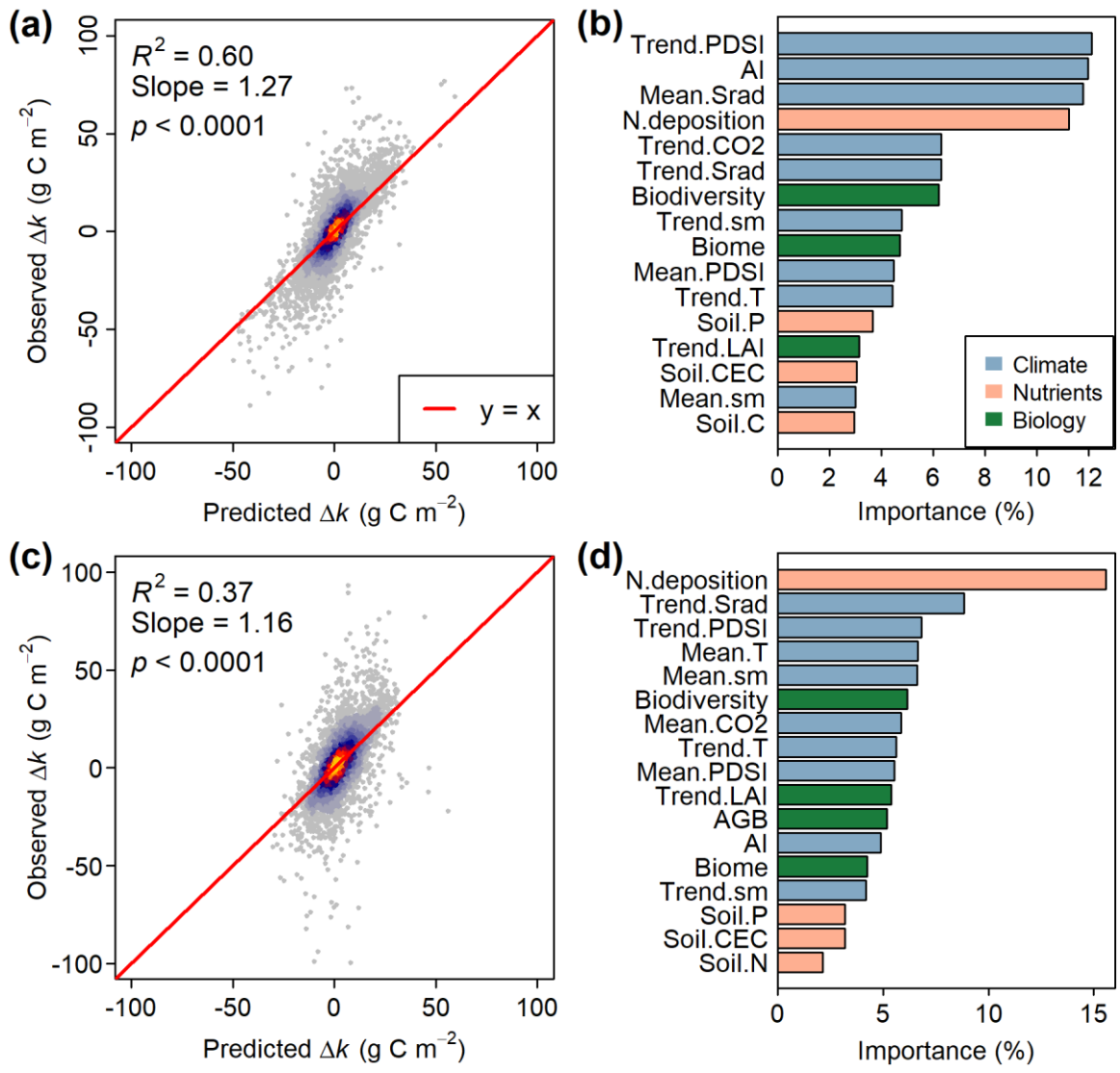

Fig. 3 Climate is the main driver of the change in drought sensitivity. (**a** and **c**) Correlations between the observed and the predicted change in sensitivity (using random forest models) for (**a**) severe droughts and (**c**) fires. There are 9989 (0.25° pixels aggregated by fact = 2) and 5358 samples for drought and fire, respectively. (**b** and **d**) The importance of drivers affecting the change in drought sensitivity for (**b**) severe droughts and (**d**) fires. The drivers are categorized into three groups: climatic (light blue), nutrient (orange), and biological (green) variables. Trend.PDSI - the slope of regression between PDSI and year, AI - aridity index, Mean.Srad - mean annual downward surface shortwave solar radiation, N.deposition - nitrogen deposition, Trend.CO_2 - the slope of regression between CO_2 concentration and year, Trend.Srad - the slope

of regression between downward surface shortwave solar radiation and year, and Trend.sm - the slope of regression between soil moisture and year.

Recovery time

The drought sensitivity reverted to pre-disturbance level approximately 4~5 years on average after disturbances. Following severe droughts, the median (mean) recovery time of the drought sensitivity was five (5.98) years, and most pixels (> 80%) recovered within nine years after the disturbances (Fig. 4a). For context with drought return intervals, historical PDSI data from 1982 to 2018 revealed a median drought return interval of 9.25 years at the global scale (Extended Data Fig. 7a), surpassing the five-year recovery time. Therefore, ecosystems would have sufficient time to return to pre-drought sensitivity. Further investigation using PDSI data from 1958 to 1981 indicated a median drought return interval of twelve years (Extended Data Fig. 7b), suggesting that severe droughts became more frequent with shorter return intervals in response to the changing climate. At the pixel level, only 6.31% (n = 341) of pixels had a recovery time longer than the current drought return intervals (based on PDSI data in 1982–2018). However, climate projections indicated further decreases in drought return intervals (Extended Data Fig. 8), reducing the time period available for ecosystems to restore their sensitivity and potentially causing permanent ecosystem changes and degradation. For fires, the median (mean) recovery time of drought sensitivity was four (4.35) years, and most pixels (> 80%) recovered within six years. The median fire return interval based on the global fire emission database[26] (GFED4.1s) burned area data (1997–2016) was 6.67 years (Extended Data Fig. 7c), which was longer than the four-year recovery time. At the pixel level, only 0.40% (n = 5) of pixels had a recovery time longer than the corresponding fire return intervals.

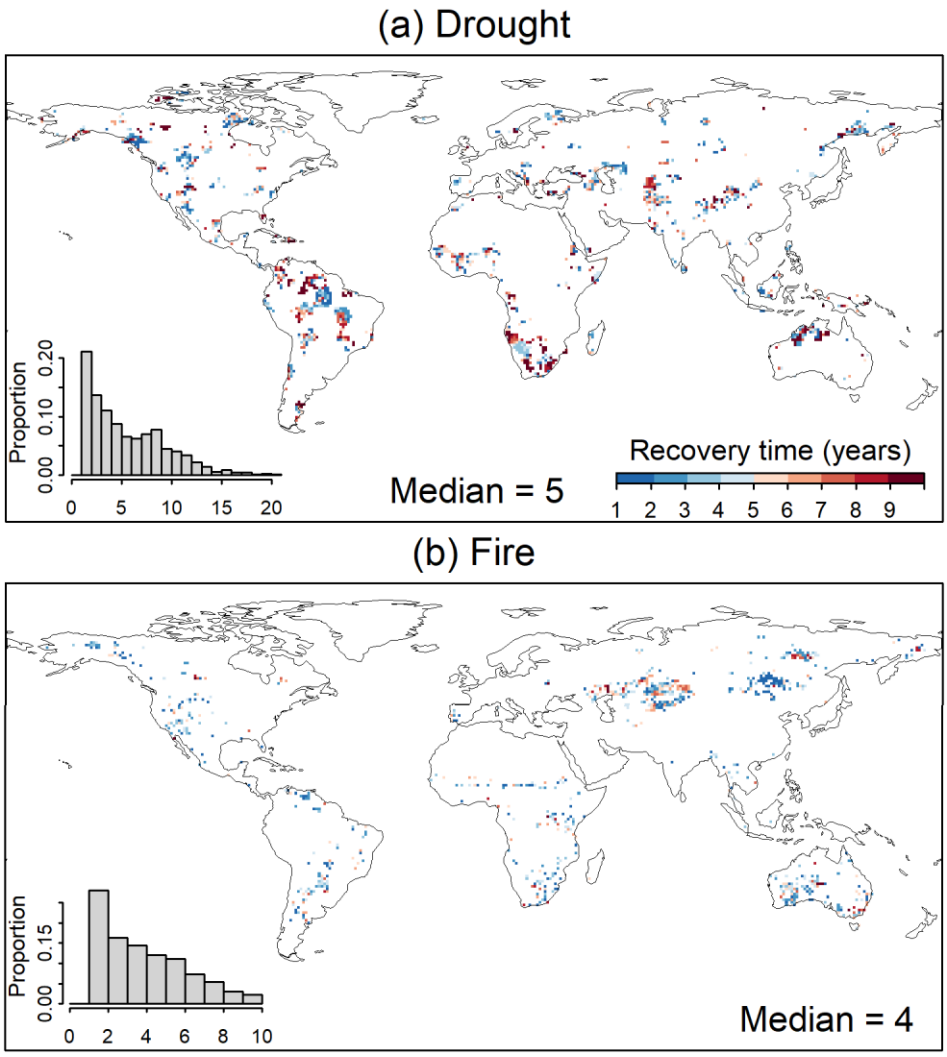

Fig. 4 Drought sensitivity recovers approximately 4~5 years after disturbances. (**a**-**b**) Distributional maps of recovery time after (**a**) severe droughts and (**b**) fires. The insets are histograms of the corresponding recovery time. There are 5407 and 1400 pixels available for drought and fire, respectively, to analyze the recovery time. The distributional maps are aggregated to 1° for visual display.

Discussion

Climate-sensitive disturbances, such as severe droughts and fires, have pronounced impacts on the productivity and functioning of terrestrial ecosystems. We quantified changes in the sensitivity of ecosystem GPP to water stress (i.e., drought sensitivity) following severe droughts and fires. Globally, changes in drought sensitivity (Δk) exhibited considerable variation across

regions, particularly in relation to aridity levels. Drought sensitivity tended to increase after disturbances in dry regions (hyperarid, arid, and semi-arid), whereas it was more likely to decrease in wet regions (i.e. humid regions). For instance, typical wet regions like tropical forests exhibited decreased sensitivity, while dry regions, such as western North America, southern Africa, and Australia, showed increased sensitivity.

Our data revealed a significant positive correlation between aridity index and biodiversity (Fig. S1a in the Supplement), capturing that wet regions generally have high biodiversity. In dry regions, biodiversity is low, and Δk is mostly greater than zero (Fig. S1b in the Supplement), signifying increased sensitivity after disturbances. Conversely, in wet regions with high biodiversity, Δk is mostly lower than zero, suggesting decreased sensitivity. We hypothesize that this reduced sensitivity in wet regions is due to the buffering effect of high species diversity, where the loss of vulnerable species is mitigated by the resilience of drought-resistant species. Wet regions, such as tropical forests, typically exhibit high species diversity[27], structural complexity, and interspecific competition. After disturbances, competition decreases[28], allowing surviving plants to access more resources, which facilitates faster ecosystem recovery. These surviving species are often more drought-tolerant[29], which could further contribute to the decreased sensitivity. Other studies have highlighted the buffering effects of biodiversity, showing that high biodiversity increases ecosystem resistance to drought[30].

In contrast, dry regions, such as Australia and western North America, have relatively low species diversity, and the buffering effects are minimal. Additionally, plants in these areas are vulnerable to water deficits due to their proximity to absolute biogeographic and climatic thresholds. For example, dryland ecosystems experience high solar radiation and temperatures, low cloud cover, and limited water availability, leading to high potential evapotranspiration and substantial water deficits. There is a significant correlation between solar radiation and aridity index (Fig. S1c in the Supplement), where high solar radiation is associated with low water availability. Consequently, dry regions with high solar radiation tend to exhibit increased sensitivity after disturbances, while wet regions with low solar radiation show marginal changes in drought sensitivity (Fig. S1d in the Supplement). Previous research has demonstrated that vegetation greenness in drylands is more sensitive to precipitation than in wet regions[31]. Similarly,

the sensitivity of leaf area index to soil moisture is much higher in water-limited regions, such as semi-arid and arid areas[32]. Our random forest models (Extended Data Fig. 5) identified low water availability, high solar radiation, and low biodiversity as the primary drivers of increased drought sensitivity in dry regions. As a result, ecosystems in dry regions are highly uncertain[33] and susceptible to future water deficits due to this increased sensitivity. We also explored the use of ecophysiological and hydrological variables to interpret our results; however, their importance was generally lower (Fig. S2 in the Supplement). This might be due to the coarse spatial resolution of the data we used, which could have decreased the significance of ecophysiological and hydrological variables. Recent research[34] also indicates that the conservative-acquisitive trade-off of plant functional traits is strong at the species scale but diminishes at the ecosystem scale.

Although drought sensitivity may change after disturbances, it can revert to its pre-disturbance condition approximately 4∼5 years on average after the disturbances. Natural ecosystems generally possess the ability to repair themselves and recover their functions, which is referred to as ecosystem resilience[35]. Currently, most ecosystems have sufficient time to restore their drought sensitivity because the recovery time is shorter than the corresponding drought return intervals (∼9 years) and fire return intervals (∼7 years). There are still 6.31% of pixels, however, exhibiting a longer recovery time than the corresponding drought return intervals, indicating that some ecosystems may not fully recover their sensitivity before the occurrence of the next drought. Based on historical PDSI data and future climate projections, drought return intervals are predicted to be shorter. The recovery of drought sensitivity will thus become challenging, particularly when the return intervals of disturbances are shorter than the required recovery time. This could impact the sustainability of terrestrial ecosystems, particularly drylands, and the capacity of terrestrial C uptake.

Disturbances sensitive to climate, such as droughts and wildfires, play critical roles in regulating ecosystem functioning and sustainability and land C sequestration. Climate change is anticipated to alter disturbance regimes and induce more severe and frequent disturbances in the following decades. Understanding and quantifying the impacts of disturbances on terrestrial ecosystems and C uptake for long-term climate change mitigation are imperative. Our findings highlight prominent changes in the sensitivity of ecosystem GPP to water stress after

290 disturbances and elucidate meaningful impacts on the recovery of the sensitivity in future
291 climates. Increased sensitivity increases the vulnerability of ecosystems to subsequent water
292 stress, and shortened disturbance return intervals impede ecosystem recovery. These long-term
293 dynamics are crucial for ecosystem sustainability, land C sinks, and global C management.

Methods

Data

Remote sensing based gross primary production (GPP) data were used to represent the productivity of ecosystems at the global scale. We used five long-term GPP products: Global Land Surface Satellite (GLASS) GPP[24], the revised eddy-covariance model of light-use efficiency (EC-LUE) based GPP[25], the near-infrared reflectance of vegetation (NIRv) based GPP[23], the P-model GPP[21,36], and the Breathing Earth System Simulator (BESS) GPP[20]. The GLASS GPP data set provided global annual GPP from 1982 to 2018 at a resolution of 0.05° using data from the Advanced Very High Resolution Radiometer (AVHRR). The GLASS GPP product was based on the EC-LUE model[37], which estimated GPP by multiplying APAR, LUE, and downregulation scalars based on flux-tower data (i.e. constraints of temperature and moisture). The reported accuracy of the EC-LUE model was R^2 = 0.61 and slope = 0.77. The revised EC-LUE GPP product provided global 8-day GPP data in 1982–2018 at a resolution of 0.05° using reanalyzed meteorological data, where APAR and LUE were split based on sunlit and shaded leaves, with atmospheric CO_2 concentration and vapor pressure deficit included in the downregulation scalars. The reported accuracy of the revised EC-LUE GPP was R^2 = 0.64 and slope = 0.70. The NIRv GPP data set provided global monthly GPP (1982–2018) at a resolution of 0.05° based on linear correlations between NIRv and GPP using the AVHRR reflectance data. The reported accuracy of the NIRv GPP was R^2 = 0.74, slope = 0.84, and RMSE = 0.93 g C m^{-2} d^{-1}. The P-model GPP data set provided global daily GPP (1982–2016) at a resolution of 0.5° using LUE models, where the LUE was predicted based on the environmental conditions (i.e. temperature, VPD, CO_2 concentration, and soil moisture content) and optimized stomatal conductance and photosynthetic rates. The reported accuracy of the P-model GPP was R^2 = 0.75, slope = 1.07, and RMSE = 1.96 g C m^{-2} d^{-1}. The latest BESS GPP (v2.0) product provided global monthly GPP data from 1982 to 2019 at a resolution of 0.05° using a data-driven process-based model that explicitly simulated canopy radiative transfer, energy balance, and photosynthesis. The reported accuracy of the BESS GPP was R^2 = 0.65, RMSE = 2.56, and bias = −0.69 g C m^{-2} d^{-1}. These GPP products were resampled to 0.25° and aggregated to the annual temporal resolution. GPP anomalies were calculated and detrended for each pixel for each GPP product. The five detrended anomalies were averaged (i.e.

to an ensemble mean) for each pixel to avoid inconsistencies and biases among the GPP products. The following analyses were based on the ensemble mean of the five anomalies in 1982–2018. We also separated the five GPP products and calculated the change in sensitivity using each product (Extended Data Fig. 1), producing comparable results.

As a supplement to remote sensing based GPP data, TRENDY-v11 GPP data[1] were used to derive the change in sensitivity. We employed eight land-surface models in TRENDY (i.e. DLEM, ISAM, LPJ, LPJ-GUESS, LPX-Bern, ORCHIDEE, VISIT, and VISIT-NIES), providing global GPP data at a resolution of 0.5° (the closest to the 0.25° resolution we used). We downloaded the GPP data under scenario S3 (containing all forcing, i.e. CO_2 concentration, climate, and land-use change), aggregated them to the annual temporal resolution, and resampled (bilinear) them to 0.25°. GPP anomalies were calculated and detrended for each pixel using GPP data from 1982 to 2018. The eight detrended GPP anomalies were averaged at the pixel level to produce an ensemble mean, which was used to derive the change in sensitivity after disturbances (Extended Data Fig. 2c and d).

We leveraged two widely used drought indices, the Palmer Drought Severity Index (PDSI)[17] and the Standardized Precipitation–Evapotranspiration Index (SPEI)[18], to indicate water stress. PDSI is a standardized metric derived from a two-layer soil water balance model, where negative and positive values indicate dry and wet conditions, respectively. We downloaded monthly 4-km historical PDSI data between 1982 and 2018 from TerraClimate[38], which were based on potential evapotranspiration (PET) derived from the Penman–Monteith equation. Monthly PDSI data were averaged to generate annual PDSI and upscaled to a resolution of 0.25°. Drought disturbances were defined as annual PDSI values below −3[17,39], which indicated severe drought. Other PDSI thresholds, such as −2 and −4, were also tested, and the results were comparable to those using −3. A threshold of −2 usually indicated moderate droughts, which had limited impacts on ecosystems. SPEI is a multi-scalar drought index that captures atmospheric water deficits by considering the difference between precipitation and PET. We aggregated monthly 4-km precipitation and PET data to 0.25° and calculated monthly SPEI12 (scale = 12-month) between 1982 and 2018 at a resolution of 0.25° using the "*SPEI*" package in R (version 4.1.3; R Core Team 2022). SPEI12 was selected because we used annual data in this study.

Monthly SPEI12 values were averaged to the annual level, and severe droughts were defined as SPEI12 values below −1.5[5,40]. Other thresholds, such as −1 and −1.2, were also tested, and the results were comparable to those using −1.5. A threshold of −1 usually indicated moderate droughts, which had limited effects on ecosystems. Global burned area data were obtained from the global fire emission database[26] (GFED4.1s), which provided monthly fractions of burned area in 1997–2016 at a 0.25° grid. We summed the monthly data to produce annual burned fractions for each grid. A fire event was defined as a burned fraction > 10%.

Future PDSI data under the Shared Socioeconomic Pathways 2-4.5 (SSP245) and 5-8.5 (SSP585)[41] were obtained from the National Center for Atmospheric Research (NCAR), which provided global PDSI data from 1900 to 2100 at a resolution of 2.5° under warming scenarios. These PDSI data were interpolated to 0.25° using the thin plate spline method implemented in the "*fields*" package in R. We also used future PDSI data from CarbonPlan[42], which provided PDSI data in 2015–2100 at a resolution of 4 km across the conterminous United States. We used this data set because it had a higher spatial resolution (than the 2.5° PDSI data). We aggregated the 4-km PDSI data to 0.25° to match the 0.25° data we used. The drought return intervals derived from the two future PDSI datasets were shown in Extended Data Fig. 8. Land-cover maps at a spatial resolution of 0.05° from the Terra and Aqua combined Moderate Resolution Imaging Spectroradiometer (MODIS) Land Cover Climate Modeling Grid (MCD12C1) Version 6 in 2001–2018 were downloaded and aggregated to 0.25°. We removed cropland and unvegetated classes (permanent wetlands, water, snow, urban, and barren) based on land-cover type 1 in MCD12C1. Pixels with land-cover changes in 2001–2018 were also removed and not used.

Derivation of changes in drought sensitivity

We used the slope of a simple linear regression between the GPP anomalies (response variable) and PDSI (predictor) to represent the sensitivity of vegetation productivity to water stress. We checked the correlation between the GPP anomalies and PDSI for each pixel (Extended Data Fig. 9a), where 50% (n = 73717) of the pixels had significant correlations (Extended Data Fig. 9b). We removed the pixels yielding non-significant correlations and compared three models, i.e. linear, quadratic, and logistic models, in modeling the GPP anomalies with PDSI for the significant pixels. As shown in Extended Data Fig. 9c, linear models were the best for 88% of the significant pixels.

Hence, we used linear models to derive the change in sensitivity for the significant pixels. Pixels that did not exhibit significant correlations between the GPP anomalies and PDSI were not used in this study. As a complementary analysis, we used multiple linear regression (using more variables as predictors), and the coefficients of PDSI from the multiple linear regression and the simple linear regression were comparable and significantly correlated (Extended Data Fig. 10). The slope of a simple linear regression between pre-drought GPP anomalies and PDSI was calculated to indicate pre-drought sensitivity (k_0). Similarly, post-drought sensitivity (k_1) was calculated using post-drought GPP anomalies and PDSI. The difference between the post- and pre-drought slopes was defined as the change in sensitivity (Δk). The same strategy was employed when using SPEI to indicate water stress. To enhance the robustness of our results, we performed multiple linear regression on annual data from 1982 to 2018, modeling GPP as a function of temperature and precipitation (i.e., GPP ~ Temperature + Precipitation) for each pixel. We calculated the residuals from this regression model for each GPP product. Next, we regressed these residuals against PDSI to determine pre-drought and post-drought sensitivities, as well as changes in sensitivity, using all available pixels (excluding those with land cover changes). The results, presented in Figs. S3 and S4 in the Supplement, were highly consistent with those obtained from detrended GPP anomalies.

$$\Delta k = k_1 - k_0 \quad (1)$$

We required at least eight years of data for regression when calculating the change in sensitivity after droughts. Eight was the first break point in the drought return intervals based on the histogram in Extended Data Fig. 7a. For fires, five years were required for regression because five was the first break point in fire return intervals (Extended Data Fig. 7c). The first drought was checked initially for each pixel, and the change in drought sensitivity was calculated using equation (1) when we had at least eight data points for the regression analysis before and after the first drought. For post-drought regression, only the GPP data between the first and the second droughts were used to avoid the interference of the second drought. Similarly, only samples between the current and the previous droughts were used for pre-drought regression. The length of pre- and post-disturbance data could vary, and we used eight years as the minimum for the regression analysis. Otherwise, the second drought would be checked. This pixel was

discarded if all droughts were not qualified for calculating the change in sensitivity. Continuous droughts were treated as one drought when deriving the changes in sensitivity. We used the first drought when two or more droughts were suitable for calculating Δk. The same procedure was applied to fires, producing the change in sensitivity after a fire event. There were 23172 and 5358 pixels available to investigate the change in sensitivity after drought and fire, respectively.

To account for spatial autocorrelations in Δk, we employed the generalized least squares (GLS) model[43] to examine the significance. We used the gls function from the "*nlme*" package in R. The exponential correlation structure, corExp, was selected to assess the significance of mean Δk by fitting the GLS models with the formula "$\Delta k \sim 1$" (regression with only the constant term). We tested five correlation structures: exponential, spherical, Gaussian, ratio, and linear. The exponential correlation structure was always ranked in the two best correlation structures for minimizing AIC. We thus decided to use the exponential correlation structure throughout the manuscript to save computational time (GLS models are extremely time-consuming when sample sizes are large). We aggregated the maps of Δk for drought disturbances using a factor of two (fact = 2) during the calculation due to the intensity of the computation, producing 9989 samples to investigate the significance. The constant term, mean Δk, was considered significant at $p < 0.05$ (two-sided) based on the GLS models and labeled with an asterisk (*).

Random forest model

Random forest regression[19], a widely used data-driven machine-learning model, was leveraged to model the change in drought sensitivity and to identify the dominant factors driving the change. Random forest regression had no statistical assumptions on data and was well-suited for analyzing high-dimensional data. We used the "*randomForest*" package in R to train the random forest model. The response variable was the change in sensitivity, Δk. The predictors included various climatic, nutrient, and biological variables, namely temperature (T), precipitation (Pr), downward surface shortwave solar radiation (Srad), PDSI, CO_2 concentration[44], the aridity index (AI)[45], soil moisture (SM), soil total nitrogen (Soil.N), soil organic carbon (Soil.C), soil organic phosphorous (Soil.P), nitrogen deposition (N.deposition), soil cation exchange capacity (Soil.CEC), plant species diversity[27] (Biodiversity), aboveground biomass (AGB)[46], the leaf area index (LAI)[47], and the biome[48] defined by the World Wildlife Fund. Climatic variables such as T, Pr, Srad, and

PDSI in 1982–2018 were obtained from TerraClimate and aggregated to a spatial resolution of 0.25° and an annual temporal resolution. The global historical data for CO_2 concentration in 1982–2013 at a resolution of 1° were resampled (bilinear) to 0.25°. The soil moisture data (0–100 cm) at a resolution of 0.1° from the European Center for Medium-Range Weather Forecasts Reanalysis v5 (ERA5) in 1982–2018 were downloaded and aggregated to 0.25°. The 8-km Global Inventory Modeling and Mapping Studies (GIMMS) LAI4g data (1982–2020) were aggregated to 0.25°. The 10-km global AGB data in 2000–2019 were aggregated to 0.25°. The 8-km Soil.N and Soil.C and 0.5° Soil.P, N.deposition, and Soil.CEC were obtained from the Oak Ridge National Laboratory Distributed Active Archive Center and resampled to 0.25°. The 95 km plant species diversity data were normalized by dividing the maximum (= $N/N_{max}\times100\%$) and resampled (bilinear) to 0.25°. The 1 km aridity index (high and low values indicate wet and dry conditions, respectively) data were aggregated to 0.25°.

We calculated the long-term mean (e.g. Mean.T, mean annual temperature) and trend (e.g. Trend.T; slope of a simple linear regression between temperature and year) of variables with more than thirty years of records for each pixel, including T, Pr, Srad, PDSI, CO_2, SM, and LAI. Both the long-term mean and the trend were used as predictors. Average AGB in 2000–2019 was used as a predictor, but no trend was calculated because the duration was less than thirty years. No trends were derived for static variables such as AI, Soil.N, Soil.P, and Biodiversity. We established separate random forest models for drought and fire disturbances because the drivers varied. Prior to training the models, highly correlated predictors were removed. For example, when mean annual precipitation and mean annual soil moisture exhibited a high correlation ($|r| > 0.7$), the predictor presenting a lower correlation with Δk was eliminated. We used 500 decision trees in the random forest models to save computation time and maintain the accuracy, and the number of splits was determined as the square root of the number of selected predictors ($\lfloor\sqrt{n}\rfloor$), which is commonly used when training random forest models. We used Shapley values[49] derived from the "*fastshap*" package in R to illustrate the responses of Δk to the predictors. Shapley values represent the contribution of each predictor by subtracting the impacts of other predictors. Shapley values can help to explain the predictions from machine-learning models and identify the relationships between the response variable and the predictors. Predictor

importance was determined by the mean absolute Shapley value of each predictor, which was normalized by dividing the sum of the mean absolute Shapley value from all predictors multiplied by 100% (Fig. 3). The dependence of Δk (i.e. Shapley values) on the predictors was shown in Extended Data Figs. 5 and 6 for drought and fire, respectively.

Estimation of recovery time

The recovery time of drought sensitivity was determined as the time required for the sensitivity to return to its pre-disturbance level. Ecosystems may need years to restore the sensitivity because it could increase significantly after disturbance. To derive the recovery time of the sensitivity, we selected pixels with a long post-disturbance time, i.e. at least sixteen and ten years for droughts and fires, respectively, ensuring a minimum of two independent regression periods. A moving-window strategy using eight-year (five-year) intervals for droughts (fires), was employed to calculate post-disturbance sensitivity for each selected pixel. The sensitivity in each moving window (e.g. 1–8, 2–9, and 3–10 years) was determined as the slope of a simple linear regression between the GPP anomalies and PDSI. For $\Delta k > 0$, the sensitivity was considered to have recovered when the post-disturbance sensitivity was equal to or lower than the pre-disturbance sensitivity (k_0) because the two sensitivities may not always be equal exactly. The recovery time was defined as the first year in the moving window in which the post-disturbance sensitivity was $\leq k_0$ (Fig. S5a in the Supplement). Likewise, when the sensitivity decreased ($\Delta k < 0$) after disturbances, the recovery time was defined as the first year in the moving window in which the post-disturbance sensitivity was $\geq k_0$ (Fig. S5b in the Supplement). There were 5407 and 1400 pixels available for drought and fire, respectively, to analyze the recovery time (Fig. 4).

Caveats

There are inherent uncertainties associated with the remote sensing GPP products and the projections of future PDSI. The five remote sensing GPP products are developed using different assumptions, models, and inputs, leading to varied results when calculating the change in sensitivity (Figs. 2 and S1). In this study, we utilize the ensemble mean of the five GPP products to mitigate uncertainties, although it may still be insufficient. Furthermore, the future PDSI data from NCAR have a coarse spatial resolution (2.5°), which does not align with the 0.25° data we

use, and the future PDSI data from CarbonPlan only cover the contiguous United States, limiting their applicability. Nevertheless, to our knowledge, these two PDSI datasets are the only long-term ones available for future warming scenarios (i.e., SSP245 and SSP585). Additionally, these future PDSI data may not precisely reflect future drought changes because they do not account for the effects of increasing CO_2 on stomatal conductance and WUE[50]. However, recent research has indicated that the effects of CO_2 on increasing WUE likely have saturated since 2000 due to increased VPD[22]. These findings highlight the challenges of accurately projecting future drought disturbances.

Data availability

The GLASS GPP data are from http://www.glass.umd.edu/Download.html. The EC-LUE GPP data are from: https://doi.org/10.6084/m9.figshare.8942336.v3. The NIRv GPP data are from: https://doi.org/10.6084/m9.figshare.12981977.v2. The P-model GPP data are from: https://zenodo.org/records/1423484. The BESS (v2.0) GPP data are from: https://www.environment.snu.ac.kr/data. The TRENDY-v11 GPP data are from: https://blogs.exeter.ac.uk/trendy/. The historical PDSI data and the climatic data (temperature, precipitation, and downward shortwave solar radiation) are from TerraClimate: https://www.climatologylab.org/terraclimate.html. Future PDSI data are from NCAR (https://rda.ucar.edu/datasets/ds299.0/) and CarbonPlan (https://carbonplan.org/). The GFED4.1s burned area data are available at https://www.globalfiredata.org/index.html. The MODIS land-cover maps are from Earthdata: https://www.earthdata.nasa.gov/.

Global data for the aridity index are from: https://doi.org/10.6084/m9.figshare.7504448.v6. Global soil moisture (0–100 cm) data are downloaded from ERA5-land: https://cds.climate.copernicus.eu/cdsapp#!/search?type=dataset. GIMMS LAI4g data are from: https://zenodo.org/records/7649108. CO_2 data are from: https://zenodo.org/records/5021361. Global data for soil total nitrogen and soil organic carbon (0–100 cm) are from: https://daac.ornl.gov/SOILS/guides/IGBP-SurfaceProducts.html. Soil organic phosphorus (0–50 cm) data are from: https://daac.ornl.gov/SOILS/guides/Global_Phosphorus_Dist_Map.html. Soil cation exchange capacity and nitrogen deposition data are from:

https://daac.ornl.gov/NACP/guides/NACP_MsTMIP_Model_Driver.html. AGB data are from: https://zenodo.org/records/4161694. The biodiversity data are from: https://anthroecology.org/anthromes/plantbiodiversity/.

Code availability

All analysis was done in the open-source software R version 4.1.3. The code is available from figshare: https://figshare.com/s/98e4dc3fdf22d3bc348c

Author contributions

M.L. and W.R.L.A. conceptualized, designed, and improved the study with input from all co-authors. M.L. wrote the initial draft, and J.P., A.T.T., G.V.G., L.Y., and W.R.L.A. discussed the design, analyses and results and provided extensive and valuable comments and revisions.

Acknowledgements

This study was supported by the Wilkes Center at the University of Utah, with thanks to the Anderegg lab. We also thank the TRENDY team. J.P. was supported by the TED2021-132627B-I00 grant funded by MCIN and the European Union NextGeneration EU/PRTR and by the CIVP20A6621 grant funded by the Fundación Ramón Areces. A.T.T. acknowledges funding from National Science Foundation grants 2003205, 2017949, and 2216855, from the University of California Laboratory Fees Research Program Award No. LFR-20-652467, and from the Gordon and Betty Moore Foundation grant GBMF11974. W.R.L.A. acknowledges support from the David and Lucille Packard Foundation and US National Science Foundation grants 1802880, 2003017, and 2044937. G.V.G. acknowledges support from the NOAA Climate and Global Change postdoctoral fellowship administered by UCAR's Cooperative Programs for the Advancement of Earth System Science (CPAESS) under the NOAA Science Collaboration Program Award #NA21OAR4310383.

Competing interests

The authors declare no competing interests.

Ethics & Inclusion statement

This research involves collaborations of scientists in both America and Spain. All authors contribute to the study design, analysis, and results, and their names are listed in the title page. All data are publicly available from online resources. This is a global study, and no local partners or agencies are required. The authors declare no competing interests and agree on the roles and responsibilities related to this study. This research is not restricted or prohibited in the setting of the researchers. No animals, discrimination, health issues, or biological materials are relevant to this research.

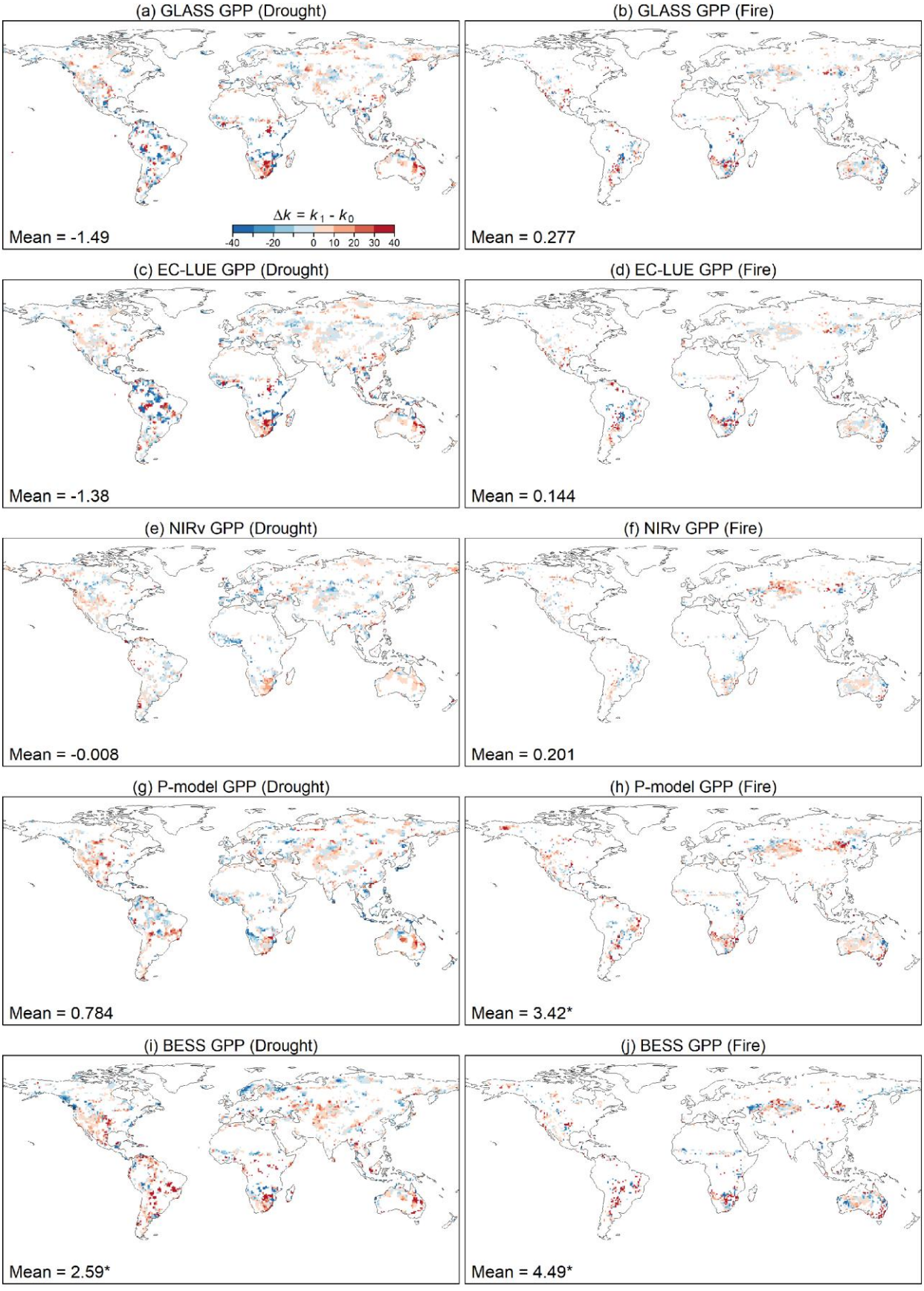
(a) GLASS GPP (Drought)
Mean = -1.49
$\Delta k = k_1 - k_0$
-40 -20 0 10 20 30 40
(b) GLASS GPP (Fire)
Mean = 0.277
(c) EC-LUE GPP (Drought)
Mean = -1.38
(d) EC-LUE GPP (Fire)
Mean = 0.144
(e) NIRv GPP (Drought)
Mean = -0.008
(f) NIRv GPP (Fire)
Mean = 0.201
(g) P-model GPP (Drought)
Mean = 0.784
(h) P-model GPP (Fire)
Mean = 3.42*
(i) BESS GPP (Drought)
Mean = 2.59*
(j) BESS GPP (Fire)
Mean = 4.49*

559

Extended Data Fig. 1 Change in drought sensitivity using the five remote sensing GPP products separately. The change in drought sensitivity after disturbances is derived from each GPP product using PDSI to indicate water stress. The distributional maps are aggregated to a resolution of 1° for visual display. *, $p < 0.05$ based on the GLS models.

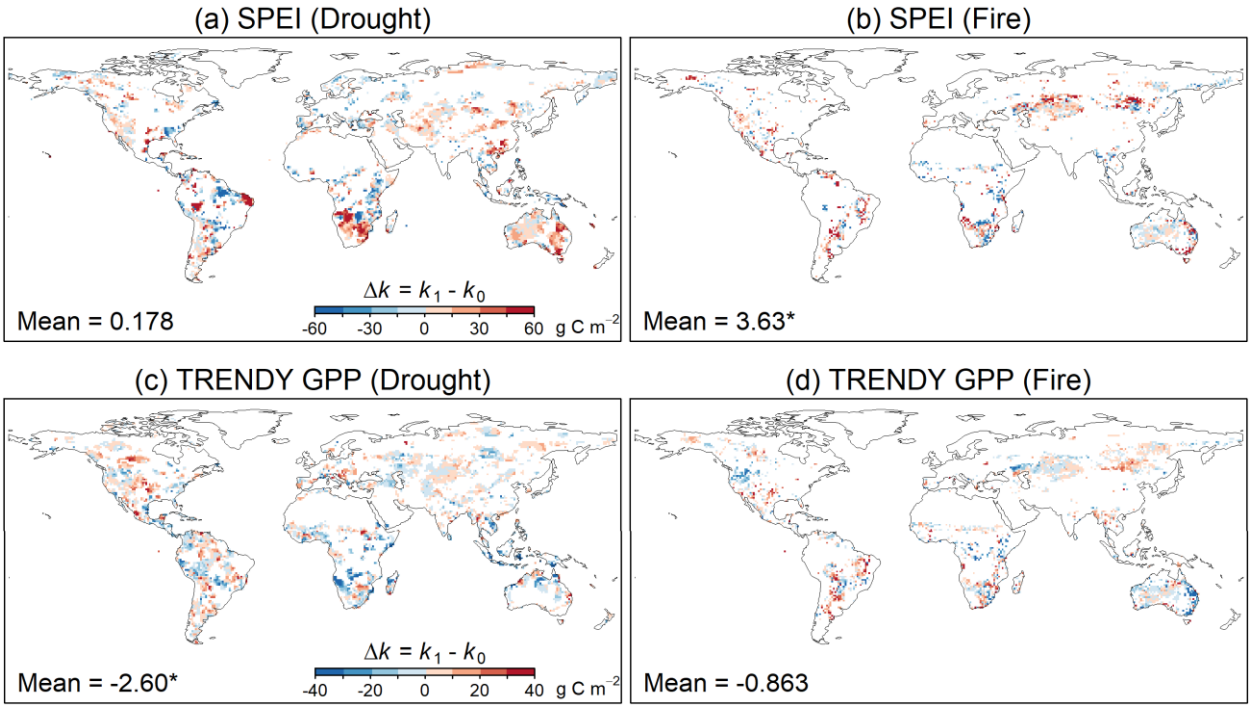

Extended Data Fig. 2 Change in drought sensitivity based on SPEI and TRENDY GPP data. (**a**-**b**) The changes in drought sensitivity after (**a**) severe droughts and (**b**) fires using SPEI to indicate water stress (remote sensing GPP regressed by SPEI). (**c**-**d**) The changes in drought sensitivity using TRENDY GPP (regressed by PDSI). The distributional maps are aggregated to 1° for visual display. *, $p < 0.05$ based on the GLS models.

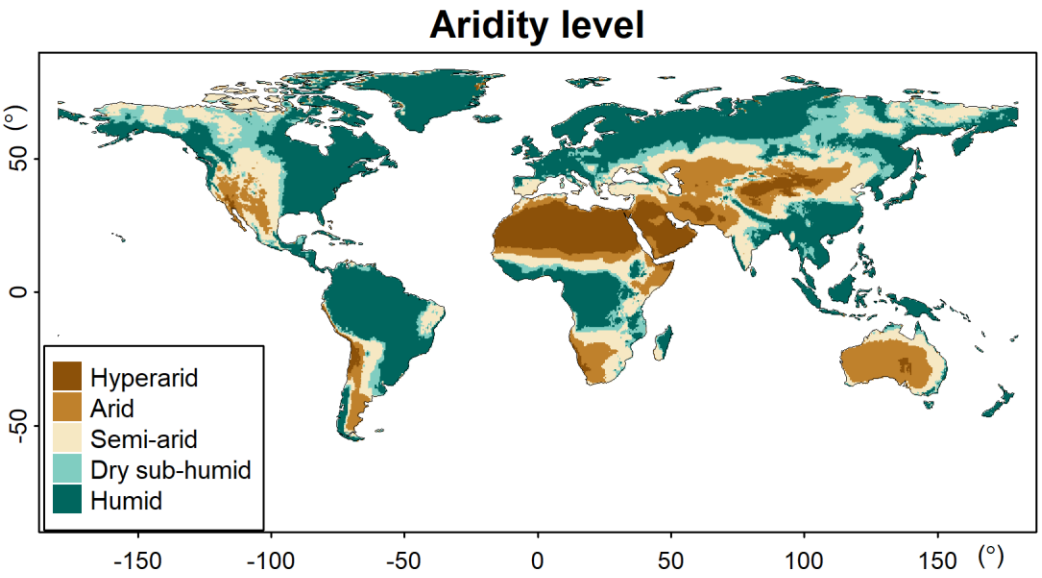

570

571 **Extended Data Fig. 3 Distribution of the aridity levels.** The aridity levels are defined based on
572 the aridity index (AI): hyperarid (AI < 0.05), arid (AI < 0.2), semi-arid (AI < 0.5), dry sub-humid (AI
573 < 0.65), and humid (AI ≥ 0.65)[33].

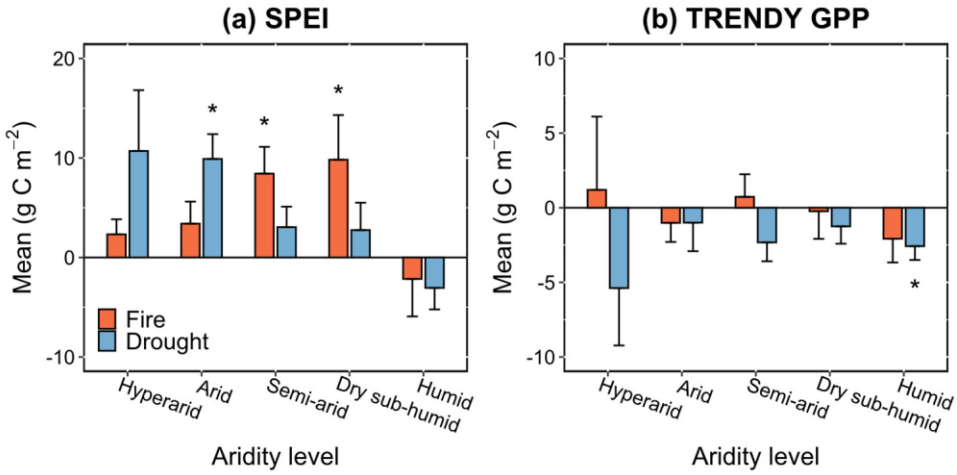

574

575 **Extended Data Fig. 4 Changes in drought sensitivity in the aridity levels when using SPEI and**
576 **TRENDY GPP.** (**a**) The change in drought sensitivity using SPEI to indicate water stress (remote
577 sensing GPP regressed by SPEI). (**b**) The change in drought sensitivity using TRENDY GPP data
578 (regressed by PDSI). Error bars are one standard error. *, $p < 0.05$ based on the GLS models.

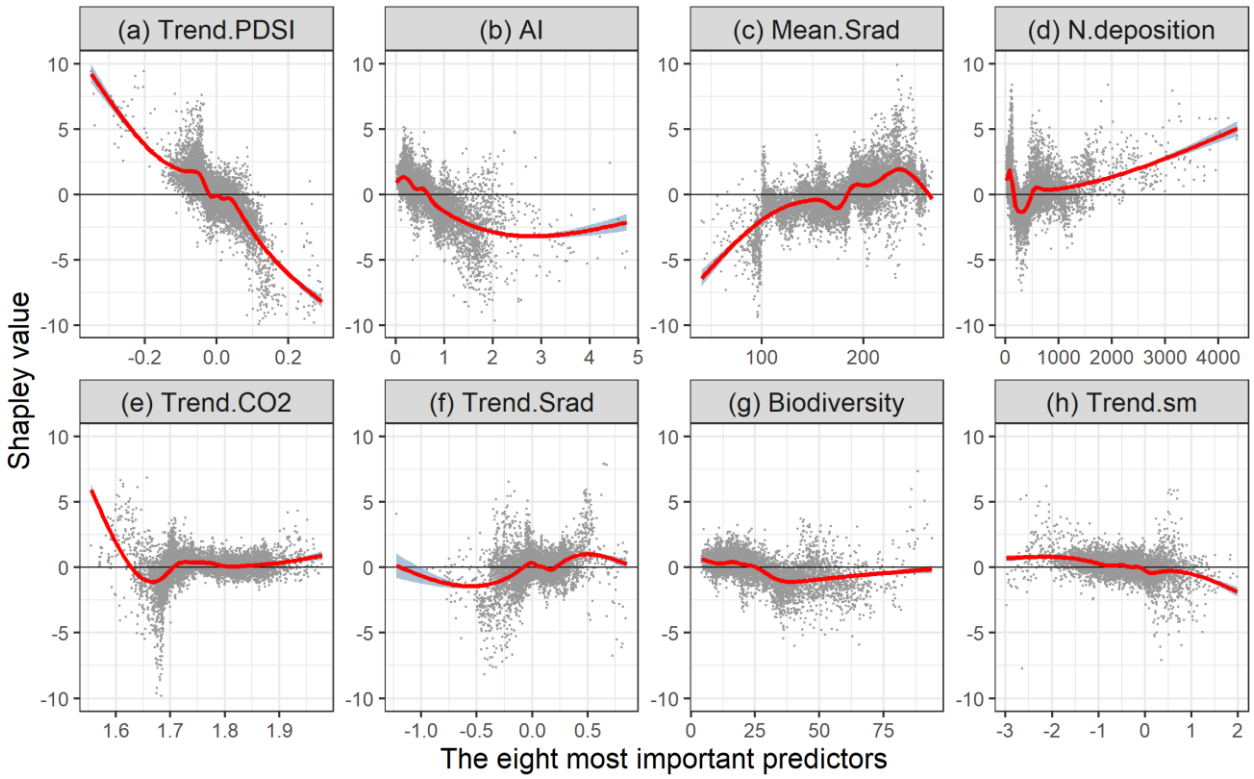

Extended Data Fig. 5 Response of the change in drought sensitivity to the most important predictors for severe droughts. The eight most important predictors are shown, where the red lines are the smoothing curves fitted by generalized additive models in the "ggplot2" package in R, and the shading represents uncertainties. The Shapley value indicates the response of the change in sensitivity to the predictors.

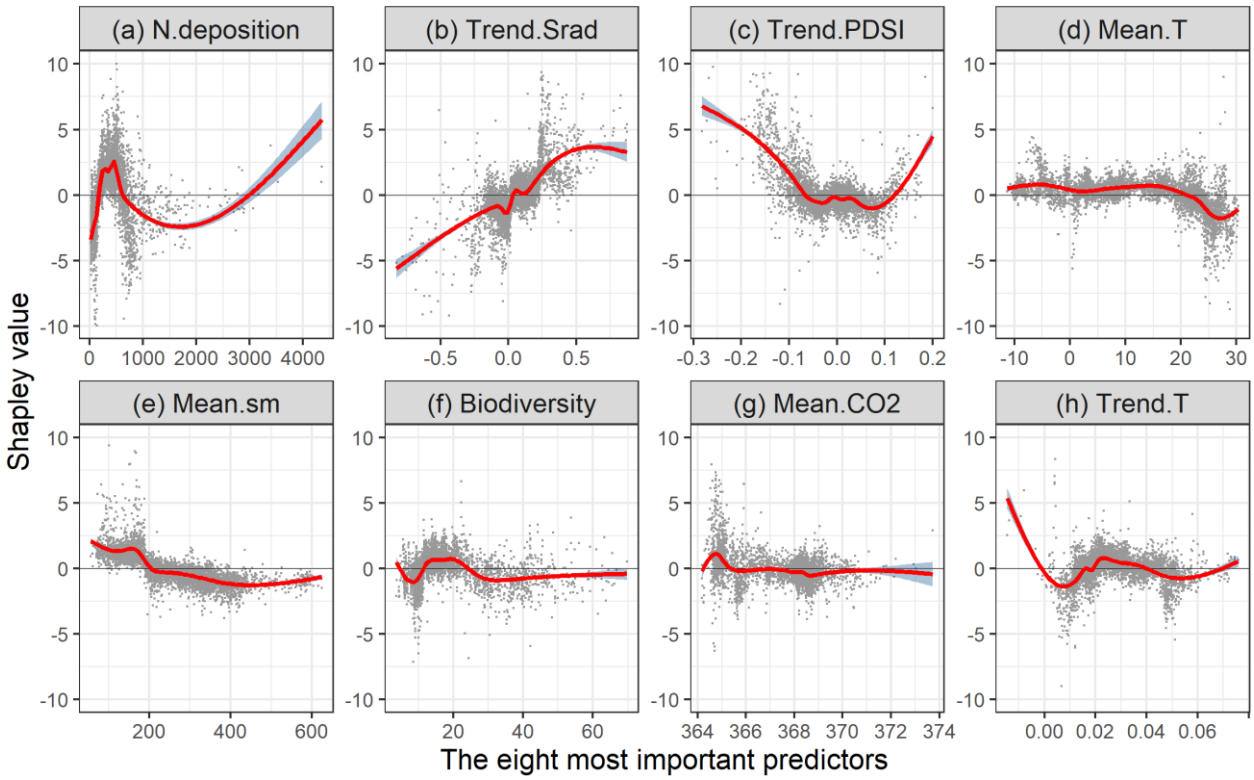

585

586 **Extended Data Fig. 6 Response of the change in drought sensitivity to the most important**
587 **predictors for fires**. The eight most important predictors are shown, where the red lines are the
588 smoothing curves fitted by generalized additive models in the "ggplot2" package in R, and the
589 shading represents uncertainties. The Shapley value indicates the response of the change in
590 sensitivity to the predictors.

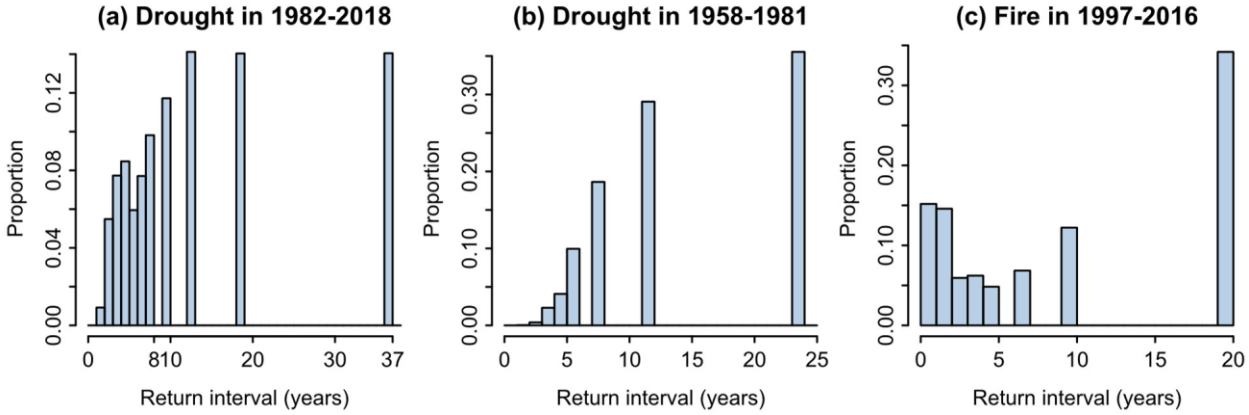

591

592 **Extended Data Fig. 7 Return intervals of severe droughts and fires**. (**a**-**b**) Drought return intervals
593 using historical PDSI data in (**a**) 1982–2018 and (**b**) 1958–1981. (**c**) Fire return intervals using the

burned area from GFED 4.1s. The bin width is one year. The median return intervals for panels (**a**-**c**) are 9.25, 12.0, and 6.67 years, respectively.

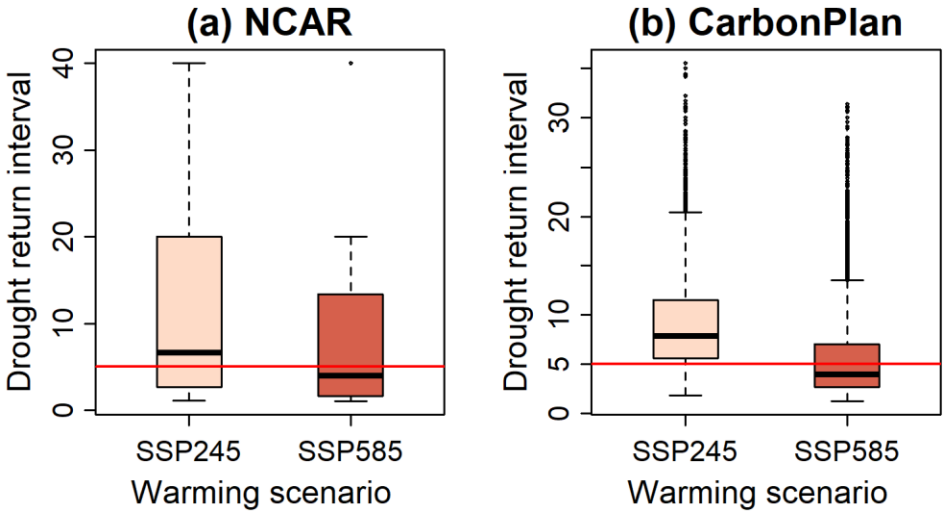

Extended Data Fig. 8 Drought return intervals using future PDSI data in 2061–2100. Boxplots of drought return intervals based on PDSI from (**a**) NCAR and (**b**) CarbonPlan under SSP245 and SSP585. The solid lines indicate the recovery time (five years after severe droughts). Box plot lines represent the interquartile range (IQR) and median, respectively, whereas the whiskers represent 1.5 times IQR (or the minimum/maximum).

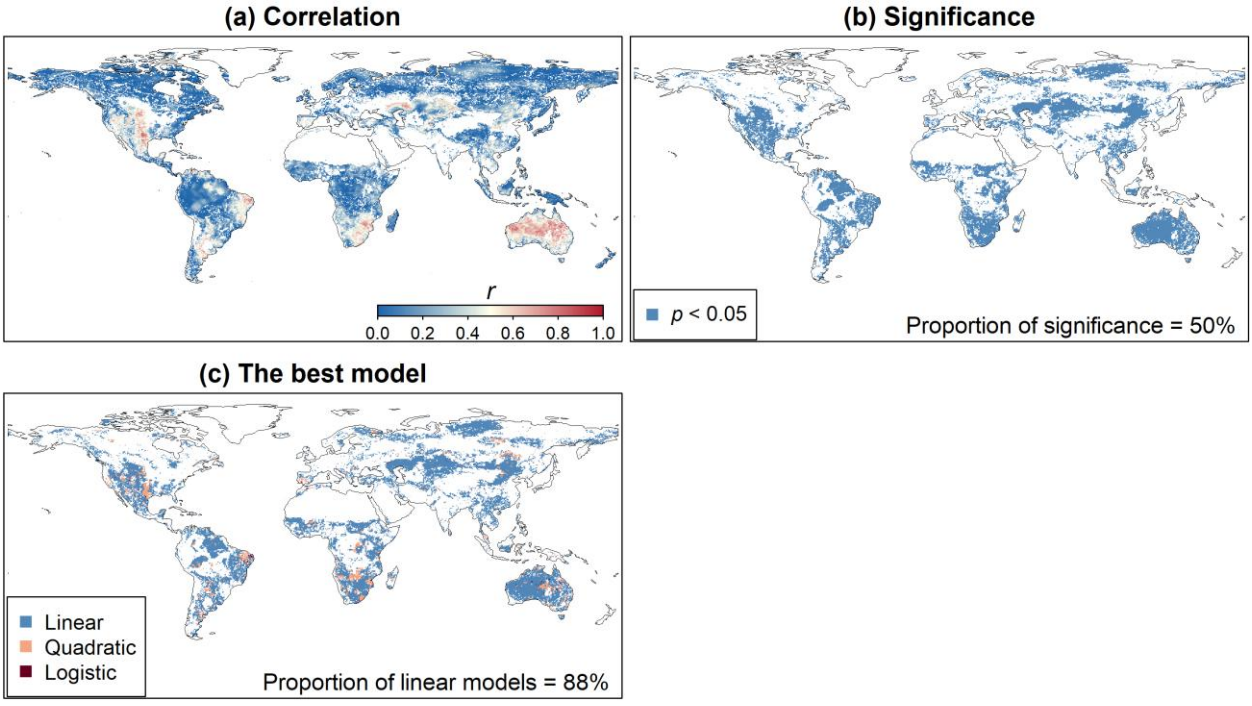

Extended Data Fig. 9 The best model at the global scale. (**a**) Correlations between the GPP anomalies and PDSI. (**b**) The distribution of pixels with significant correlations (50% of pixels indicating significant correlations). There are 146210 and 73717 pixels in panels (**a**) and (**b**), respectively. (**c**) The best model for the significant pixels, where there are three models: linear (blue), quadratic (orange), and logistic (red) models. The best model is defined as the model with minimum Akaike Information Criterion (AIC) and significant regression coefficients (e.g. the linear model is used when the quadratic term in the quadratic model is not significant). The linear model is the best for 88% of the pixels.

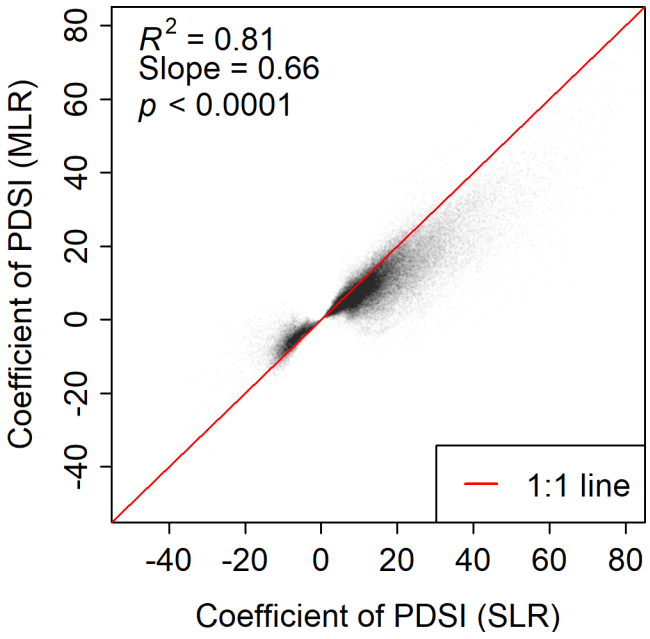

Extended Data Fig. 10 Results of simple linear regression (SLR) and multiple linear regression (MLR) are comparable. Scatter plot of the coefficients (i.e. sensitivity) of PDSI from SLR ($GPP_{anomaly} \sim PDSI$) and MLR ($GPP_{anomaly} \sim Srad_{anomaly} + T_{anomaly} + PDSI$) based on data in 1982–2018. Each dot is a pixel, and only pixels with significant correaltions between $GPP_{anomaly}$ and PDSI are shown. There are 84.85% of pixels exhibiting positive correlations between GPP anomalies and PDSI.

References

1. Friedlingstein, P. *et al.* Global Carbon Budget 2022. *Earth System Science Data* **14**, 4811–4900 (2022).
2. Dai, A. Drought under global warming: a review. *WIREs Climate Change* **2**, 45–65 (2011).
3. Parks, S. A. & Abatzoglou, J. T. Warmer and Drier Fire Seasons Contribute to Increases in Area Burned at High Severity in Western US Forests From 1985 to 2017. *Geophysical Research Letters* **47**, e2020GL089858 (2020).
4. Ciais, P. *et al.* Europe-wide reduction in primary productivity caused by the heat and drought in 2003. *Nature* **437**, 529–533 (2005).
5. van der Woude, A. M. *et al.* Temperature extremes of 2022 reduced carbon uptake by forests in Europe. *Nat Commun* **14**, 6218 (2023).
6. Anderegg, W. R. L. *et al.* Tree mortality from drought, insects, and their interactions in a changing climate. *New Phytologist* **208**, 674–683 (2015).
7. Anderegg, W. R. L. *et al.* A climate risk analysis of Earth's forests in the 21st century. *Science* **377**, 1099–1103 (2022).
8. Penuelas, J. Decreasing efficiency and slowdown of the increase in terrestrial carbon-sink activity. *One Earth* **6**, 591–594 (2023).
9. Cooper, L. A., Ballantyne, A. P., Holden, Z. A. & Landguth, E. L. Disturbance impacts on land surface temperature and gross primary productivity in the western United States. *Journal of Geophysical Research: Biogeosciences* **122**, 930–946 (2017).
10. Frank, D. *et al.* Effects of climate extremes on the terrestrial carbon cycle: concepts, processes and potential future impacts. *Global Change Biology* **21**, 2861–2880 (2015).

11. Anderegg, W. R. L. *et al.* Pervasive drought legacies in forest ecosystems and their implications for carbon cycle models. *Science* **349**, 528–532 (2015).

12. Fu, Z. *et al.* Atmospheric dryness reduces photosynthesis along a large range of soil water deficits. *Nat Commun* **13**, 989 (2022).

13. Flack-Prain, S., Meir, P., Malhi, Y., Smallman, T. L. & Williams, M. The importance of physiological, structural and trait responses to drought stress in driving spatial and temporal variation in GPP across Amazon forests. *Biogeosciences* **16**, 4463–4484 (2019).

14. Zhang, Y. *et al.* Canopy and physiological controls of GPP during drought and heat wave. *Geophysical Research Letters* **43**, 3325–3333 (2016).

15. Detto, M. & Pacala, S. W. Plant hydraulics, stomatal control and the response of a tropical forest to water stress over multiple temporal scales. *Global Change Biology* **n/a**, (2022).

16. Liu, M., Trugman, A. T., Peñuelas, J. & Anderegg, W. R. L. Climate-driven disturbances amplify forest drought sensitivity. *Nat. Clim. Chang.* 1–7 (2024) doi:10.1038/s41558-024-02022-1.

17. Palmer, W. C. Meteorological drought. *U.s.department of Commerce Weather Bureau* (1965).

18. Beguería, S., Vicente-Serrano, S. M., Reig, F. & Latorre, B. Standardized precipitation evapotranspiration index (SPEI) revisited: parameter fitting, evapotranspiration models, tools, datasets and drought monitoring. *International Journal of Climatology* **34**, 3001–3023 (2014).

19. Breiman, L. Random Forests. *Machine Learning* **45**, 5–32 (2001).

20. Li, B. *et al.* BESSv2.0: A satellite-based and coupled-process model for quantifying long-term global land–atmosphere fluxes. *Remote Sensing of Environment* **295**, 113696 (2023).

21. Stocker, B. D. *et al.* P-model v1.0: an optimality-based light use efficiency model for simulating ecosystem gross primary production. *Geoscientific Model Development* **13**, 1545–1581 (2020).

22. Li, F. *et al.* Global water use efficiency saturation due to increased vapor pressure deficit. *Science* **381**, 672–677 (2023).

23. Wang, S., Zhang, Y., Ju, W., Qiu, B. & Zhang, Z. Tracking the seasonal and inter-annual variations of global gross primary production during last four decades using satellite near-infrared reflectance data. *The Science of The Total Environment* **755**, 142569 (2020).

24. Liang, S. *et al.* The Global Land Surface Satellite (GLASS) Product Suite. *Bulletin of the American Meteorological Society* **102**, E323–E337 (2021).

25. Zheng, Y. *et al.* Improved estimate of global gross primary production for reproducing its long-term variation, 1982–2017. *Earth System Science Data* **12**, 2725–2746 (2020).

26. van der Werf, G. R. *et al.* Global fire emissions estimates during 1997–2016. *Earth System Science Data* **9**, 697–720 (2017).

27. Ellis, E. C., Antill, E. C. & Kreft, H. All Is Not Loss: Plant Biodiversity in the Anthropocene. *PLOS ONE* **7**, e30535 (2012).

28. Sheil, D. Disturbance and distributions: avoiding exclusion in a warming world. *Ecology and Society* **21**, (2016).

29. Feeley, K. J., Davies, S. J., Perez, R., Hubbell, S. P. & Foster, R. B. Directional changes in the species composition of a tropical forest. *Ecology* **92**, 871–882 (2011).

30. Isbell, F. *et al.* Biodiversity increases the resistance of ecosystem productivity to climate extremes. *Nature* **526**, 574–577 (2015).

31. Zhang, Y. *et al.* Increasing sensitivity of dryland vegetation greenness to precipitation due to rising atmospheric CO2. *Nat Commun* **13**, 4875 (2022).

32. Li, W. *et al.* Widespread increasing vegetation sensitivity to soil moisture. *Nat Commun* **13**, 3959 (2022).

33. Wang, L. *et al.* Dryland productivity under a changing climate. *Nat. Clim. Chang.* **12**, 981–994 (2022).

34. Anderegg, W. R. L., Martinez-Vilalta, J., Mencuccini, M. & Poyatos, R. Community assembly influences plant trait economic spectra and functional trade-offs at ecosystem scales. *Proceedings of the National Academy of Sciences* **121**, e2404034121 (2024).

35. Pimm, S. L. The complexity and stability of ecosystems. *Nature* **307**, 321–326 (1984).

36. Stocker, B. D. *et al.* Drought impacts on terrestrial primary production underestimated by satellite monitoring. *Nat. Geosci.* **12**, 264–270 (2019).

37. Yuan, W. *et al.* Global estimates of evapotranspiration and gross primary production based on MODIS and global meteorology data. *Remote Sensing of Environment* **114**, 1416–1431 (2010).

38. Abatzoglou, J. T., Dobrowski, S. Z., Parks, S. A. & Hegewisch, K. C. TerraClimate, a high-resolution global dataset of monthly climate and climatic water balance from 1958–2015. *Sci Data* **5**, 170191 (2018).

39. van der Schrier, G., Barichivich, J., Briffa, K. R. & Jones, P. D. A scPDSI-based global data set of dry and wet spells for 1901–2009. *Journal of Geophysical Research: Atmospheres* **118**, 4025–4048 (2013).

40. Anderegg, W. R. L., Trugman, A. T., Badgley, G., Konings, A. G. & Shaw, J. Divergent forest sensitivity to repeated extreme droughts. *Nat. Clim. Chang.* **10**, 1091–1095 (2020).

41. Dai, A. Dai Global Palmer Drought Severity Index (PDSI). UCAR/NCAR - Research Data Archive https://doi.org/10.5065/D6QF8R93 (2017).

42. Anderegg, W. R. L. *et al.* Future climate risks from stress, insects and fire across US forests. *Ecology Letters* **25**, 1510–1520 (2022).

43. Aitken, A. C. On Least Squares and Linear Combination of Observations. *Proceedings of the Royal Society of Edinburgh* **55**, 42–48 (1936).

44. Cheng, W. *et al.* Global monthly gridded atmospheric carbon dioxide concentrations under the historical and future scenarios. *Sci Data* **9**, 83 (2022).

45. Zomer, R. J., Xu, J. & Trabucco, A. Version 3 of the Global Aridity Index and Potential Evapotranspiration Database. *Sci Data* **9**, 409 (2022).

46. Xu, L. *et al.* Changes in global terrestrial live biomass over the 21st century. *Science Advances* **7**, eabe9829 (2021).

47. Cao, S. *et al.* Spatiotemporally consistent global dataset of the GIMMS Leaf Area Index (GIMMS LAI4g) from 1982 to 2020. *Earth System Science Data Discussions* 1–31 (2023) doi:10.5194/essd-2023-68.

48. Olson, D. M. *et al.* Terrestrial Ecoregions of the World: A New Map of Life on Earth. *bisi* **51**, 933–938 (2001).

49. Štrumbelj, E. & Kononenko, I. Explaining prediction models and individual predictions with feature contributions. *Knowl Inf Syst* **41**, 647–665 (2014).

727 50. Swann, A. L. S., Hoffman, F. M., Koven, C. D. & Randerson, J. T. Plant responses to
728 increasing CO2 reduce estimates of climate impacts on drought severity. *Proceedings of the*
729 *National Academy of Sciences* **113**, 10019–10024 (2016).
730